A multitransitional molecular and atomic line study of S:140

Astron. Astrophys. 277, 595–608 (1993)

ASTRONOMY AND ASTROPHYSICS

A multi-transitional molecular and atomic line study of S140

Nigel R. Minchin [1], **Glenn J. White** [1], **and Rachael Padman** [2]

[1] Department of Physics, Queen Mary and Westfield College, University of London, Mile End Road, London E1 3NS, UK
[2] Mullard Radio Astronomy Observatory, Cavendish Laboratory, Madingley Road, Cambridge CB3 0HE, UK

Received February 17, accepted May 12,, 1993

Abstract. We present high-angular resolution maps of the S140 molecular cloud in various transitions of the ^{12}CO, ^{13}CO and C^{18}O molecules and single-channel observations of the $^3P_1 \rightarrow {}^3P_0$ line of neutral atomic carbon (CI). Velocity channel maps of the ^{12}CO lines show a systematic shift of the emission peak away from the outflow source with increasing velocity offset from the line centre. The blue and redshifted outflow lobes are separated by ~35 arcsec (0.15 pc) in projection and the outflow axis is believed to be directed close to the observers' line-of-sight. The masses of the blue and redshifted outflow lobes were found to be 19.5 and 8.1$M_\odot$ respectively, giving a total mass for the outflow of 27.6$M_\odot$. The higher J-level ^{12}CO lines are strongly self-absorbed, with the amount of self-absorption varying with position across the mapped region.

All the ^{12}CO, ^{13}CO and C^{18}O lines show enhanced main beam brightness temperatures at the molecular cloud/HII region interface. The ^{13}CO line intensities imply the excitation temperature increases from ~65-70K at the position of the outflow source, to ~250K at the interface region. The CI emission is mainly confined to a clumpy, elongated ridge-like feature adjacent to the edge of the molecular cloud and is coincident with a similar feature seen in ^{12}CO line emission. The coincidence of these features contradicts homogeneous cloud models and is interpreted as evidence that the molecular material is composed of dense clumps interspersed with a more tenuous interclump medium. A second region of intense CI emission is located inside a ring of CS emission, implying that ^{12}CO here is dissociated by the radiation field from the embedded infrared cluster and *not* the external radiation field. Observed positions on the PDR have significantly higher values of $T_{\rm mb}$(CI)/$T_{\rm mb}$(^{13}CO) than for the general cloud, implying N(CI)/N(^{13}CO) is likely to be significantly higher for positions on the PDR than in the general molecular cloud.

Key words: stars: early-type – interstellar medium: HII regions – ISM: radio lines: interstellar – jets and outflows – ISM: individual objects: S140

1. Introduction

The complex consisting of the Lynds 1204 dark cloud and the adjacent S140 HII region lies at a distance of 910 pc (Crampton & Fisher 1974). The molecular cloud lies to the northeast of a bright H_α rim (Blair et al. 1978), excited by the nearby (~2 pc) B0 star HD 211880. Within the molecular cloud is an embedded cluster of three infrared sources (IRS 1, 2 and 3) lying only 70-80 arcsec from the molecular cloud/HII region interface (Beichman et al. 1979; Hackwell et al. 1982). Previous authors have referred to the molecular cloud core containing the embedded sources as S140; throughout this paper we will do the same.

The first detailed molecular line studies of S140 were reported by Blair et al. (1978). They noted broad and asymmetric line profiles at the position of the ^{12}CO peak, and a sharp dropoff in the ^{12}CO intensity to the southwest (adjacent to the H_α rim). Subsequent ^{12}CO observations identified a high-velocity bipolar molecular outflow (Bally & Lada 1983; Snell et al. 1984b). High resolution observations of the ^{12}CO J = 1→0 line imply a 35 arcsec separation between the blue and red lobes, aligned along the northwest-southeast direction (Hayashi et al. 1987). Of the three infrared sources in the embedded cluster, only IRS 1 lies on the line connecting the centroids of the blue and red ^{12}CO emission peaks. This, coupled with the fact that IRS1 is by far the most luminous of the three sources in the far-infrared and radio continuum, has led to the conclusion that it is the most probable source of the high-velocity molecular outflow.

There are relatively few well-studied molecular clouds with associated edge-illuminated ionization fronts, e.g. S155-Cepheus B (see Minchin et al. 1992 and references therein) and M17 (see Stutzki et al. 1988 and references therein). Most previous line and continuum observations of S140 have been unable to distinguish adequately between the outflow and molecular cloud/HII region interface due to the lack of angular resolution (often ≥1 arcmin) compared to the separation between these features (70-80 arcsec). This means the position and structure of the photo-dissociation region (PDR) is still poorly understood. For this reason we have mapped various transitions of the ^{12}CO, ^{13}CO and C^{18}O molecules and the $^3P_1 \rightarrow {}^3P_0$ line of neutral atomic carbon (CI) at high-angular resolution (9-22 arcsec). Comparison of this comprehensive data set with previous

Table 1. Spectral lines observed

Species	Transition	Freq. (GHz)	Beam (arcsec)	η_{mb}
^{12}CO	J = 2→1	230.538	21	0.55
^{12}CO	J = 3→2	345.796	14	0.55
^{12}CO	J = 4→3	461.041	10	0.39
^{13}CO	J = 2→1	220.399	22	0.6
^{13}CO	J = 3→2	330.588	15	0.55
$C^{18}O$	J = 3→2	329.331	15	0.55
CI	$^3P_1 \rightarrow {}^3P_0$	492.161	9	0.39

line and continuum observations permits the first detailed discussion of this complex region.

2. Observations

The observations were obtained between November 1987 and April 1992, using the James Clerk Maxwell Telescope[1] (JCMT), located on Mauna Kea, Hawaii. The observing details are given in Table 1. The ^{12}CO, ^{13}CO and $C^{18}O$ observations were obtained using receivers A1 (200-280 GHz) and B2 (330-360 GHz) (both Schottky mixer systems) and these were used in conjunction with an acousto-optical spectrometer (White 1988). The telescope was operated in position switching mode, with an off-source reference 10 arcmin to the south and the east. Pointing errors were less than 5 arcsec at all frequencies.

The neutral carbon (CI) and ^{12}CO J = 4→3 observations were obtained using Receiver C1, a dual-polarization heterodyne receiver with InSb detectors (Padman et al. 1992). A new mapping technique was used for the CI observations, with the local oscillator frequency being held constant and the telescope raster scanned in azimuth, whilst simultaneously beam-switching in the scan direction using the nutating sub-reflector. Several such dual-beam maps of S140 were made, with different parallactic angles and chopper throws to give good coverage in two-dimensional fourier space. These maps were then processed using a maximum-entropy algorithm (DBMEM, see Richer 1992) to give the final RA-Dec map. The DBMEM reconstruction process attempts to deconvolve the dual-beam response function from the observed maps. A fuller description of the CI observational technique and the data processing is given in White & Padman (1991). The $C^{18}O$ J = 3→2 observations consist of 8 spectra, starting at the (0,0) position and spaced apart by 10 arcsec, along a line running due southwest across the molecular cloud/HII region interface. For the rest of the paper this line will be referred to as the 'southwestern cut'.

The results presented in this paper have been calibrated in units of corrected main-beam brightness temperature T_{mb} (= T_A^*/η_{mb}) and as such have been corrected for all atmospheric, ohmic, scattering and spillover losses. Also included is a first-order correction for sideband gains of the particular mixers. From observations of Mars we found the beam size for the CI observations to be 9 arcsec and η_{mb} = 0.39±0.04. The centre position (0,0) for each of the maps is $\alpha_{1950} = 22^h\ 17^m\ 42^s$, $\delta_{1950} = 63^o\ 3'\ 45''$.

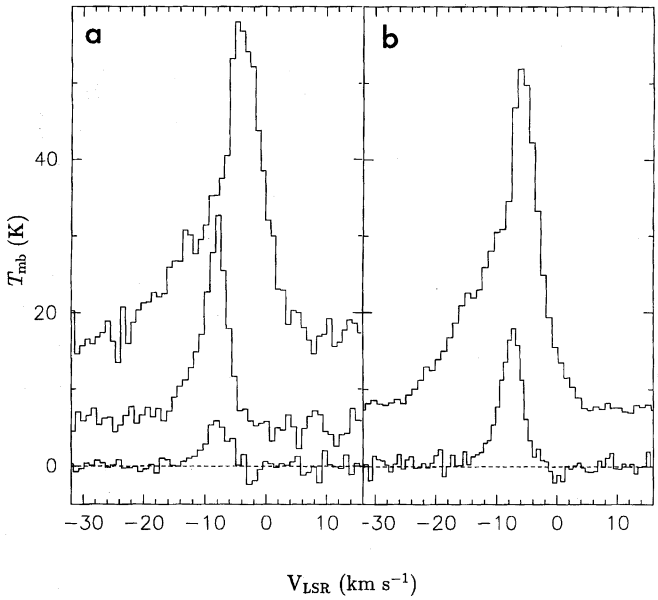

Fig. 1. Line profiles of the (a) ^{12}CO (offset by +15K), ^{13}CO (offset by +5K) and $C^{18}O$ J = 3→2 transition (b) ^{12}CO (offset by +5K), and ^{13}CO J = 2→1 transition from the (0,0) position of the S140 maps

3. Results

In Fig. 1 we show the line profiles of the J = 3→2 transitions of ^{12}CO, ^{13}CO and $C^{18}O$ and the J = 2→1 transition of ^{12}CO and ^{13}CO at the (0,0) position. The peak values of T_{mb} for the ^{12}CO J = 2→1 and J = 3→2 lines are 44±1K and 41±1.5K respectively, distinctly higher than the T_R value of 29K reported for the ^{12}CO J = 1→0 line (Hayashi et al. 1987) in a similar beamsize (16 arcsec compared to 21 arcsec and 14 arcsec respectively). The ^{13}CO lines have peak values of T_{mb} = 18.5±1K and 28±1.5K respectively. Therefore, unlike ^{12}CO, the highest value of peak T_{mb} is observed in the J = 3→2 transition. For the $C^{18}O$ J = 3→2 line the value of T_{mb} for the emission peak is 5.9±0.8K.

The ^{12}CO J = 2→1 and 3→2 line profiles are strikingly similar to those of the J = 1→0 transition at the same position (Hayashi et al. 1987). Both the ^{12}CO lines are broad, $\Delta V \sim 30$ km s^{-1}, extending from V_{LSR} = -24 to 6 km s^{-1}, with prominent

[1] The James Clerk Maxwell Telescope is operated by the Royal Observatory, Edinburgh, on behalf of the SERC, the Netherlands Organisation for Pure Research, and the National Research Council of Canada.

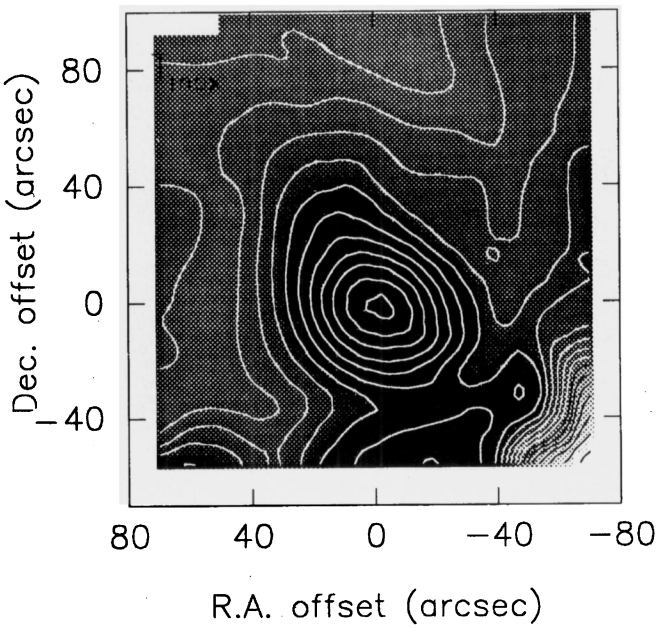

Fig. 2. Greyscale image, with isophotal contours overlaid, of the peak main beam brightness temperature for the ^{12}CO J = 2→1 transition. The base level contour is at 4.5K and the contour interval is 2K. The grid spacing is 15 arcsec and the total number of data points is 113

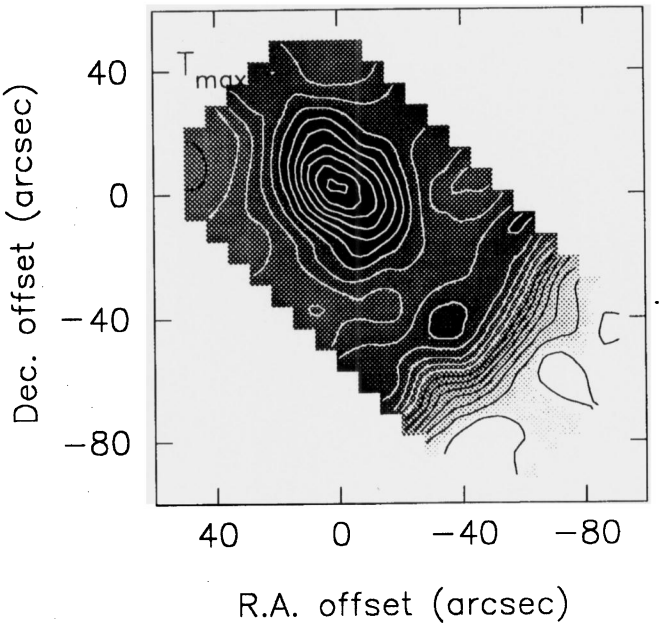

Fig. 3. Greyscale image, with isophotal contours overlaid, of the peak main beam brightness temperature for the ^{12}CO J = 3→2 transition. The base level contour is at 3.5K and the contour interval is 2K. The grid spacing is 7 arcsec and the total number of data points is 105

blue wings and the emission peak at ∼ -8 km s^{-1}. Such strong similarities are not to be found between the ^{13}CO line profiles. Hayashi et al. (1987) noted that the ^{13}CO J = 1→0 line profile is symmetric, whereas our ^{13}CO J = 2→1 and 3→2 spectra show the presence of broad blue wings, which are most prominent on the 3→2 line. This is most likely due to the optical depth increasing with frequency, as expected for a species thermalized at a temperature greater than ∼E_u/k. In Sect. 4.3.2 we show that τ(^{12}CO 3→2) > τ(^{12}CO 2→1) (0.54 as compared to 0.32, assuming T_{kin}∼67K). As the observed main beam brightness temperatures are a function of both T_{ex} and τ along the line-of-sight, it will be difficult to observe the wings of a line (where the optical depth is considerably lower than at the velocity of peak emission) for a transition that does not already have a considerable optical depth at the emission peak. This also explains why the line widths observed for ^{12}CO transitions are far greater than for optically thinner isotopes. There is no evidence of a blue wing on the C^{18}O J = 3→2 line, but, as the optical depth of this isotope is a factor of 5-10 lower than for ^{13}CO, this is to be expected. There is a striking velocity difference between the peaks of the J = 3→2 ^{12}CO and the ^{13}CO and C^{18}O transitions, with the ^{12}CO line peaking at -5 km s^{-1}, while the ^{13}CO and C^{18}O lines peak at -8 km s^{-1}. This is discussed further in Sect. 4.2.

Figures 2 and 3 show the peak ^{12}CO J = 2→1 and 3→2 main beam brightness temperature over the mapped region. For both transitions the temperature peak occurs slightly north of the (0,0) position, close to the infrared sources IRS1 and 3 (Hackwell et al. 1982). There is a steep decrease in T_{mb} between 60 and 80 arcsec to the southwest of the peak, coincident with the position of the molecular cloud/HII region interface (as delineated by the H_α map shown in Hayashi et al. 1985). Adjacent to the edge of the molecular cloud is an elongated ridge where T_{mb} is enhanced relative to the region 10-20 arcsec northeast of the ridge and the general cloud temperatures. The ridge feature is most prominent and elongated in the J = 3→2 map (Fig. 3).

Velocity channel maps of the ^{12}CO J = 2→1 and 3→2 integrated intensity from the mapped region are shown in Figs. 4 and 5 respectively. Both maps confirm the bipolarity of the outflow and closely resemble the ^{12}CO J = 1→0 velocity channel maps of Hayashi et al. (1987). Maps of the ^{12}CO J = 2→1 and 3→2 integrated emission in the blue and red wings are shown in Figs. 6 and 7 respectively. These maps agree closely to those already published of the ^{12}CO J = 1→0 emission (Snell et al. 1984b; Hayashi et al. 1987). The peaks of the blue and red wings are offset by ∼35 arcsec (∼0.15pc), along a line with position angle ∼-20 degrees. There is a prominent arc-like, elongated feature extending to the north of the blue wing emission peak, and both the red and blueshifted emission peaks are extended along the southwest-northeast direction. These features have also been seen in previous ^{12}CO studies (e.g. Snell et al. 1984a, 1984b; Hayashi et al. 1985, 1987).

Figure 8 is a velocity channel map of the ^{13}CO J = 2→1 integrated intensity. The emission is concentrated over a smaller velocity range than for the ^{12}CO lines, V_{LSR} = -12 to -4 km s^{-1}. These observations are at poorer angular resolution than the ^{12}CO J = 3→2 line observations (22 arcsec compared to 14 arcsec) so the morpology of the outflow is far less well defined, but it is clear there is a shift in the position of the emission peak

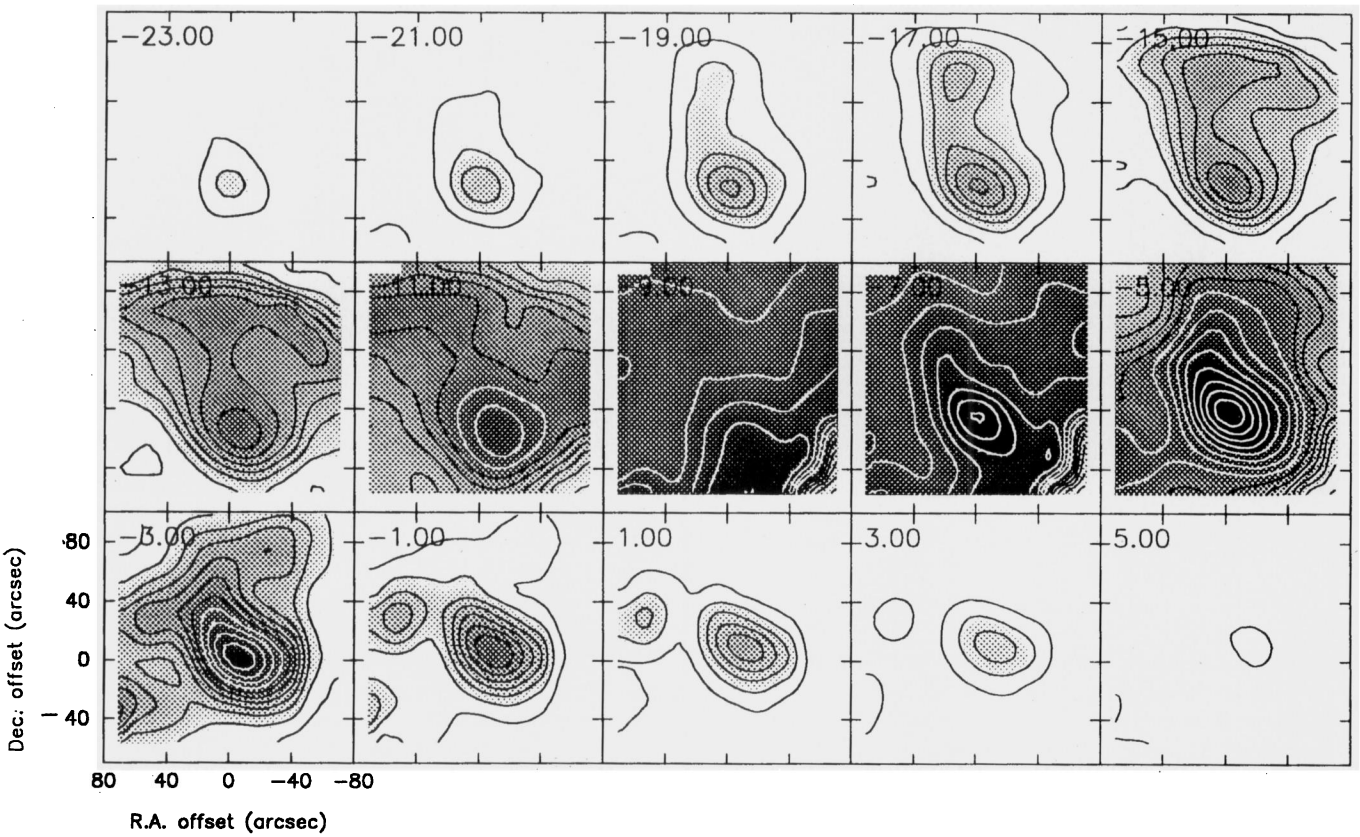

Fig. 4. Velocity channel maps of the ^{12}CO J = 2→1 integrated intensity from S140. Each map is a greyscale image with isophotal contours overlaid. The channel width is 2 km s^{-1}, the base level contour is at 2 K-km s^{-1} and the contour interval is 4 K-km s^{-1}

with velocity. As for the ^{12}CO observations, the direction of the shift is along a southeast-northwest direction.

Figure 9 shows a map of the CI $^3P_1 \rightarrow {}^3P_0$ main beam brightness temperature in a 1.3 km s^{-1} channel centred at -8 km s^{-1} (White & Padman 1991). The highest temperatures ($\leq$10K) are observed along a clumpy, elongated ridge-like feature adjacent to the edge of the molecular cloud that is between 40 and 60 arcsec from the (0,0) position and extends for ~120 arcsec along the southeast-northwest direction. Warm CI is also observed deeper into the molecular cloud, ~20-40 arcsec to the east of the (0,0) position, but not at the (0,0) position itself.

4. Discussion

4.1. The bipolar outflow

The morphology of the bipolar outflow, as seen in ^{12}CO emission, is unusually complex. The elongated blueshifted feature extending northwest from the emission peak is particularly prominent in ^{12}CO J = 2→1 emission and over 80 arcsec in length (~0.36 pc). This feature appears roughly parabolic in projection, twisting rapidly near the emission peak from northeast to due north (see Figs 4 and 6). The redshifted emission is also slightly elongated towards the north, but to a much lesser degree. This elongated, arc-like feature is prominent at the blueshifted velocities of V_{LSR} = -18 to -12 km s^{-1} and the redshifted velocities V_{LSR} = -6 to 0 km s^{-1}. Figure 6 is directly comparable with Fig. 3 of Hayashi & Murata (1992), which shows the ^{12}CO J = 2→1 emission over a similarly large area. The morphology of the outflow implied by both sets of observations is identical.

Similar bright, elongated molecular line features have been observed around other outflows and are usually interpreted as the dense walls of outflow cavities. Possibly the most famous example of this phenomenon is L1551, which has bright, parabolic-shaped features either side of the outflow source, believed to be the cavity walls where the high-velocity flow is mainly confined (e.g. Uchida et al. 1987). The clear separation of the blue and redshifted ^{12}CO outflow lobes of L1551 is in marked contrast to S140, where these features partially overlap (see Figs 6 and 7). The obvious implication is that the S140 outflow direction is close to our line-of-sight, whereas the L1551 outflow lies almost in the plane of the sky. Further evidence for this is the small separation between the emission peaks of the outflow lobes compared to the total extent of the molecular outflow (35 arcsec compared to ~150 arcsec).

Channel maps of the ^{12}CO J = 3→2 emission (Fig. 5) show a morphology for the inner 40"×40" region of the outflow that is almost identical to the ^{12}CO J = 1→0 emission, at similar spatial resolution (14 arcsec compared to 15 arcsec; see Fig. 5 of Hayashi et al. 1987). At extreme blueshifted velocities (-22 to -16 km s^{-1}) the emission peak is at offset (0,-15), moving to

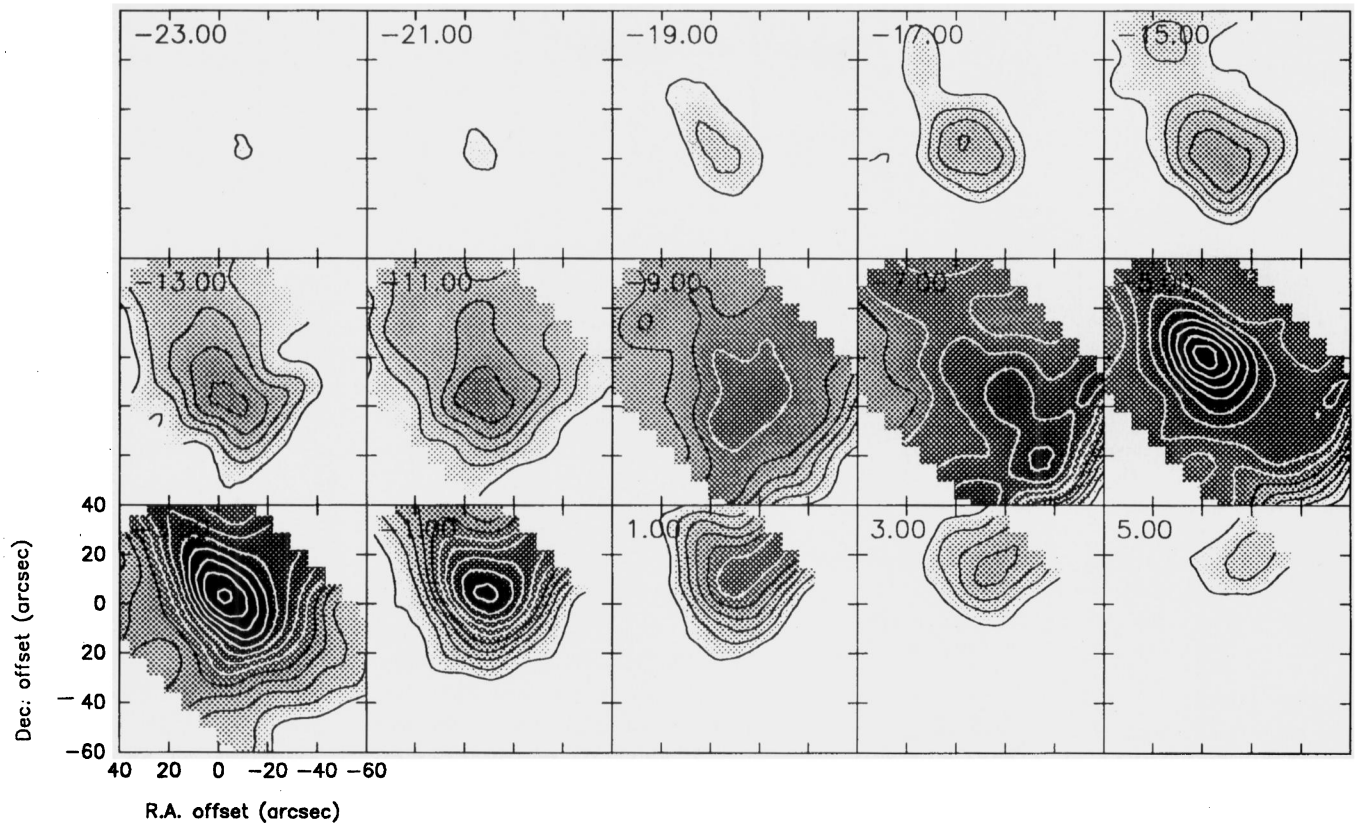

Fig. 5. Velocity channel maps of the ^{12}CO J = 3→2 integrated intensity from S140. Each map is a greyscale image with isophotal contours overlaid. The channel width is 2 km s^{-1}, the base level contour is at 2 K-km s^{-1} and the contour interval is 4 K-km s^{-1}

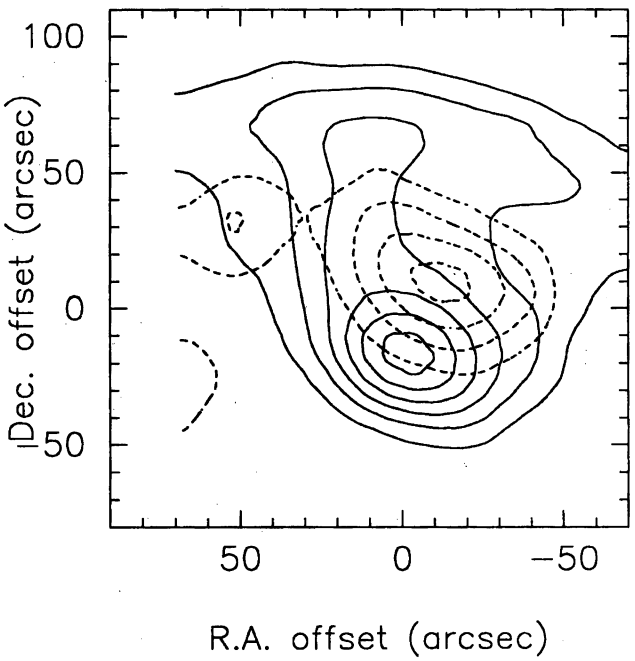

Fig. 6. A map of the integrated emission in the blue (solid contours) and redshifted (dashed contours) wings for the ^{12}CO J = 2→1 transition. The blue wing is integrated from -30 to -11 kms^{-1} and the red wing from -4 to -10 km s^{-1}. The base level contour is at 35 K-km s^{-1} and the contour interval is 25 K-km s^{-1}

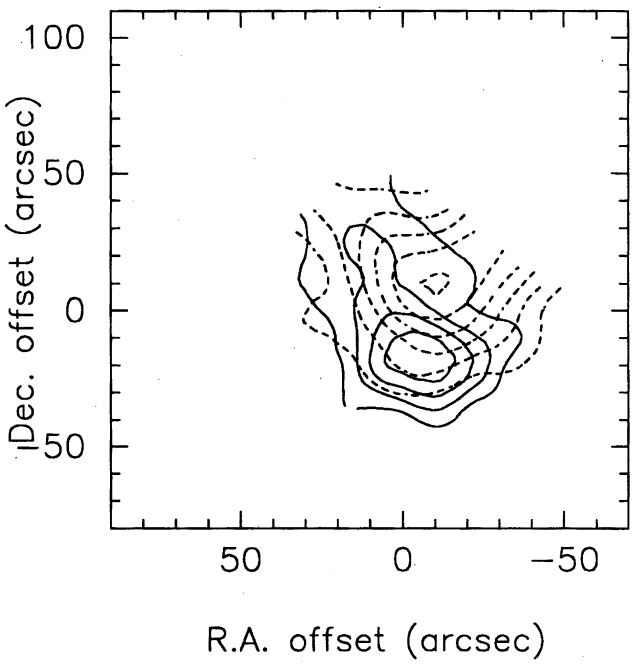

Fig. 7. A map of the integrated emission in the blue (solid contours) and redshifted (dashed contours) wings for the ^{12}CO J = 3→2 transition. The blue wing is integrated from -30 to -11 kms^{-1} and the red wing from -4 to -10 km s^{-1}. The base level contour is at 40 K-km s^{-1} and the contour interval is 30 K-km s^{-1}

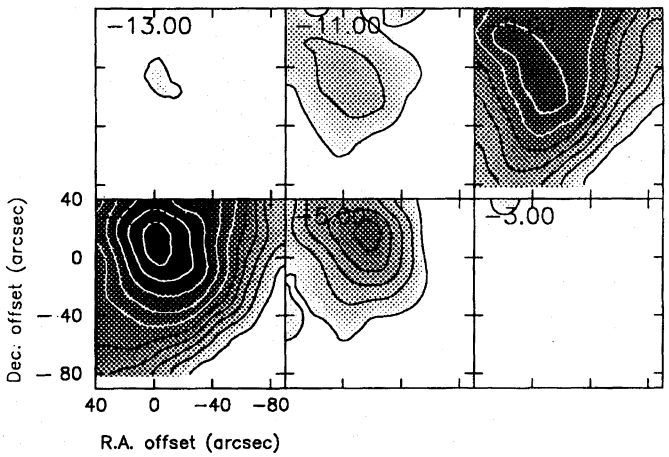

Fig. 8. Velocity channel maps of the ^{13}CO J = 3→2 integrated intensity from S140. Each map is a greyscale image with isophotal contours overlaid. The channel width is 2 km s^{-1}, the base level contour is at 3 K-km s^{-1} and the contour interval is 3 K-km s^{-1}. The grid spacing is 10 arcsec and the total number of data points is 75

the (0,0) position by V_{LSR} = -7 to -5 km s^{-1}. The peak gradually shifts to the northeast with increasing redshifted velocity, reaching (-15,+15) by V_{LSR} = 4 to 6 km s^{-1}. The systematic shift of the emission peak with velocity is characteristic of bipolar outflows and has been observed towards numerous other outflow sources, possibly representing an accelerated outflow, e.g. L1551 (Parker et al. 1991; Fridlund & White 1991). Alternatively, there may be more material at high velocity further from the outflow source, possibly due to prompt entrainment of the ^{12}CO by a neutral jet (e.g. Richer et al. 1992).

The direction of the bipolar outflow, i.e. the line connecting the emission peaks of the blue and redshifted lobes (position angle ~-20 degrees), is perpendicular to the position angle of infrared polarization (~60-80 degrees) for the outflow source (Sato et al. 1985). This is observed for several other bipolar outflows e.g. GL 2591 (Minchin et al. 1991a) and R Mon (Minchin et al. 1991b) and is attributed to either the scattering of radiation from the outflow source within a circumstellar disc or the dichroic absorption of radiation as it traverses a medium of aligned grains within the disc.

The masses of the blue and redshifted outflow lobes can be estimated from the total integrated emission across molecular line maps. Unfortunately, neither the ^{12}CO J = 3→2 or the ^{13}CO line maps fully cover the outflow region. For this reason, only the ^{12}CO J = 2→1 line map has been used for mass estimates. For the ^{12}CO J = 2→1 line, the general equation for column density (see Eq. 5) becomes

$$N(^{12}\mathrm{CO}) = \frac{T_{\mathrm{ex}}}{e^{-16.59/T_{\mathrm{ex}}}} 1.05 \times 10^{13} \int T_{\mathrm{mb}}(2 \rightarrow 1)\, dv \qquad (1)$$

where the values of the constants have been inserted and the emission is assumed to be optically thin. As the derivation of column density is based on the assumption that the lines are optically thin, we have applied a correction factor, $\beta = \tau/1 - e^{-\tau}$, to account for the high optical depths observed.

The SPECX spectral line data reduction package allows the integrated line intensity over a given area ($\int\int T_{\mathrm{mb}}(2 \rightarrow 1)\, dvdA$) to be obtained in K km s^{-1} arcsec.^{2}. This quantity can be related to the mass for ^{12}CO (following a similar derivation to that of Wilson & Mauersberger 1990) by

$$M(\mathrm{M}_\odot) = 1.01 \times 10^{-7} \frac{T_{\mathrm{ex}}}{e^{-16.59/T_{\mathrm{ex}}}} \mathrm{D}^2 \int\int T_{\mathrm{mb}}(2 \rightarrow 1) dvdA \qquad (2)$$

where a ^{12}CO/H$_2$ abundance ratio of 10^{-4} has been assumed and D is the distance to the observed region in kpc. Taking the intensity ratios of the ^{12}CO/^{13}CO emission for the 2→1 and 3→2 transitions (R) for velocities across both the blue and redshifted emission wings, gives $\tau(^{12}\mathrm{CO})$ using

$$R = \frac{1 - e^{-\tau(^{12}\mathrm{CO})}}{1 - e^{-\tau(^{13}\mathrm{CO})}} \sim [1 - e^{-\tau(^{12}\mathrm{CO})}] \frac{\mathrm{X}}{\tau(^{12}\mathrm{CO})} \qquad (3)$$

where X is the ^{12}CO/^{13}CO isotopic abundance ratio, the ^{13}CO emission is assumed to be optically thin and equal T_{ex} for both lines is assumed. Values of $\tau(^{12}\mathrm{CO})$ were derived for the emission wings at various positions across the outflow and, as for the J = 1→0 and 2→1 transitions (Snell et al. 1984b), $\tau(^{12}\mathrm{CO})$ was generally found to be between 3 and 5.

Assuming the observed quantity T_{mb} approximates to the physical quantity T_{b}, the brightness temperature, then using the definition of T_{ex} for an emission line

$$T_{\mathrm{mb}} = \frac{h\nu}{k} \frac{1}{e^{h\nu/kT_{\mathrm{ex}}} - 1} (1 - e^{-\tau}) \qquad (4)$$

the derived values of $\tau(^{12}\mathrm{CO})$ and observed values of T_{mb} imply that for the outflow wings T_{ex} ~15–20K. Again this is in reasonable agreement with the results of Snell et al. (1984b), who found T_{ex} ~12±3K. As applying Eq. (4) assumes unity filling factor, our derived temperature is a lower limit.

The derived masses of the blue (-30<V_{LSR}<-11 km s^{-1}) and redshifted (-4<V_{LSR}<10 km s^{-1}) outflow lobes are 19.5 and 8.1M$_\odot$ respectively, giving a total mass for the outflow of 27.6M$_\odot$. These values agree closely with the results of Snell et al. (1984b) for the ^{12}CO J = 1→0 transition, who found 17.0, 7.4 and 24.4M$_\odot$ respectively. Margulis & Lada (1985) found a total mass for the S140 outflow of 35 and 39M$_\odot$ using maps of the ^{13}CO J = 1→0 and J = 2→1 transitions. The discrepancy is most likely due to the fact that they used an optically thin isotope, and thus our results must be considered as lower limits.

It is remarkable that the mass within the blueshifted outflow lobe is ~2.5 times the mass in the redshifted lobe. This asymmetry was also noted by Snell et al. (1984b). There is more self-absorption of the optically thick ^{12}CO lines at redshifted rather than blueshifted velocities (see Sect. 4.2), an effect that is likely to cause a more serious underestimate for the mass of the redshifted lobe. Obviously this may exagerate the implied mass asymmetry, although Hayashi et al. (1987) estimated the mass of the outflow lobes using a map of the ^{13}CO J = 1→0 line emission and found a similar asymmetry. As there is little

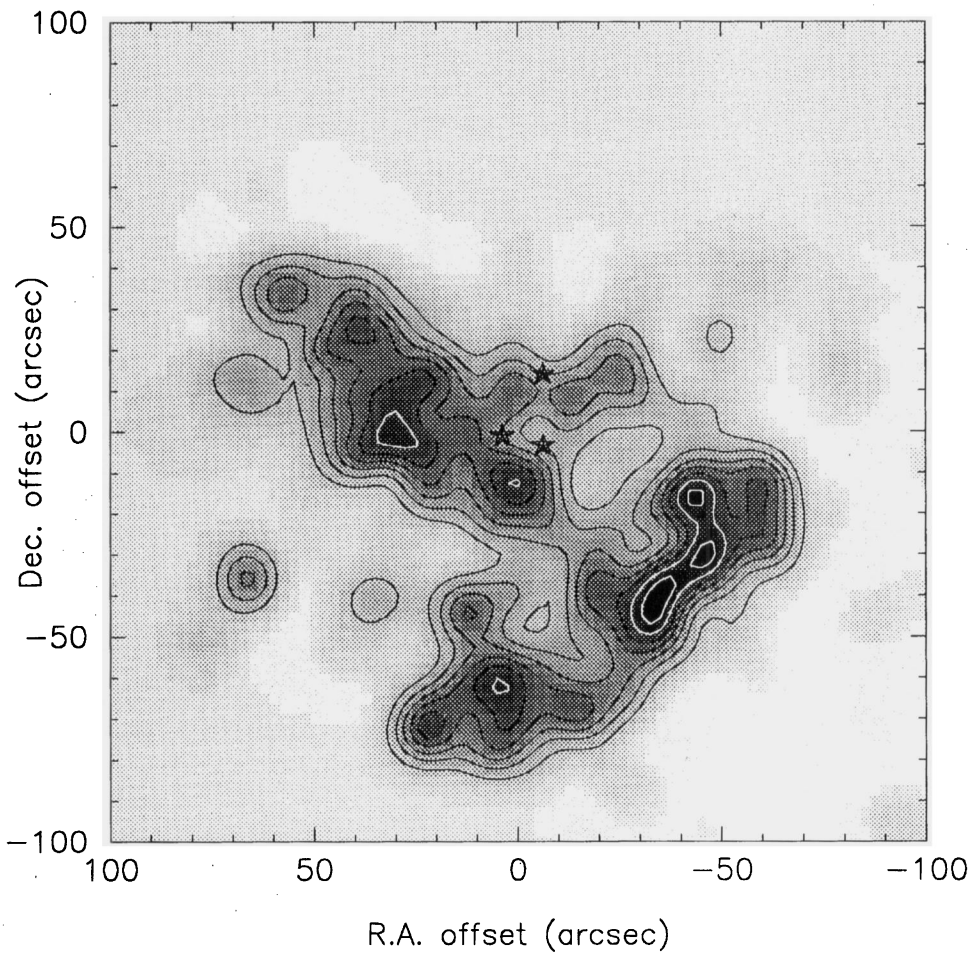

Fig. 9. Greyscale image, with isophotal contours overlaid, of the peak main beam brightness temperature for the CI $^3P_1 \rightarrow {}^3P_0$ transition in a 1.3 km s^{-1} channel centred at -8 km s^{-1}. The base level contour is at 1K and the contour interval is 1K. The positions of the three infrared sources are shown as five-pointed stars

or no self-absorption of optically thin ^{13}CO line emission (as shown by the ^{13}CO spectra in Fig. 1), this implies that the mass asymmetry is indeed real.

4.2. Line profiles

As mentioned in Sect. 3, for the J = 3→2 spectra at the (0,0) position there is a distinct shift between V_{max} for the ^{12}CO line (-5 km s^{-1}) compared to that for the ^{13}CO and C^{18}O lines (-8 km s^{-1}). Close examination of Fig. 1(a) shows the velocity offset between V_{max} for the ^{12}CO and ^{13}CO J = 2→1 spectra at this position to be minimal (<1 km s^{-1}). Previous observations of this position in S140 show there to be little or no velocity offset between V_{max} for the ^{12}CO and ^{13}CO J = 1→0 lines and confirm our observation that this is also the case for the J = 2→1 lines (Snell et al. 1984b; Hayashi et al. 1987). The lower resolution observations of Phillips et al. (1988) confirm the velocity offset of V_{max} for the ^{12}CO J = 3→2 line relative to that for the lower J level ^{12}CO transitions.

The obvious question is whether this velocity offset from the V_{LSR} of the molecular cloud (-8 km s^{-1}) is unique to the ^{12}CO J = 3→2 line, or is also the case for higher J level transitions. Figure 10 shows line profiles for the ^{12}CO J = 3→2 and 4→3 transitions at the (0,0) position and several nearby offsets. For both the J = 3→2 and 4→3 spectra V_{max} is consistently at a V_{LSR} of between -4 and -5 km s^{-1}, demonstrating that the velocity offset is also present in the J = 4→3 transition.

Such shifts in V_{max} for higher ^{12}CO lines (compared to the lower lying and optically thin isotope lines) have also been observed towards other regions of intense line emission in molecular clouds e.g. Orion and NGC 2024 (Graf et al. 1990); S106 and DR21 (White et al. 1986) and NGC 2071 (Snell et al. 1984b). As in these objects, the apparent velocity shift is most likely due to self-absorption of the optically thick high J ^{12}CO lines by foreground material with a lower T_{ex}. The ^{12}CO J = 2→1, 3→2 and 4→3 spectra (Figs. 1 and 10) at the (0,0) position each show a secondary peak at between V_{LSR} = -15 to -13 km s^{-1} and a sharp drop in intensity to the blueshifted side of V_{max}. Self-absorption tends to produce steep-sided dips in the spectral profile and double peaked spectra. This has also been observed in ^{12}CO 2→1, 3→2, 4→3 and 7→6 spectra towards DR21 (White et al. 1986; Jaffe et al. 1989).

Clearly the self-absorption is centred at $V_{LSR} \sim$ -8 km s^{-1}, where it is most pronounced, and is present over the velocity range -4 < V_{LSR} < -13 km s^{-1}. Emission from material at a certain velocity can only be absorbed by foreground material at the same velocity, but if the self-absorption is completely due to the foreground cloud material the implied velocity range (-4 < V_{LSR} < -13 km s^{-1}) of the material would suggest the molec-

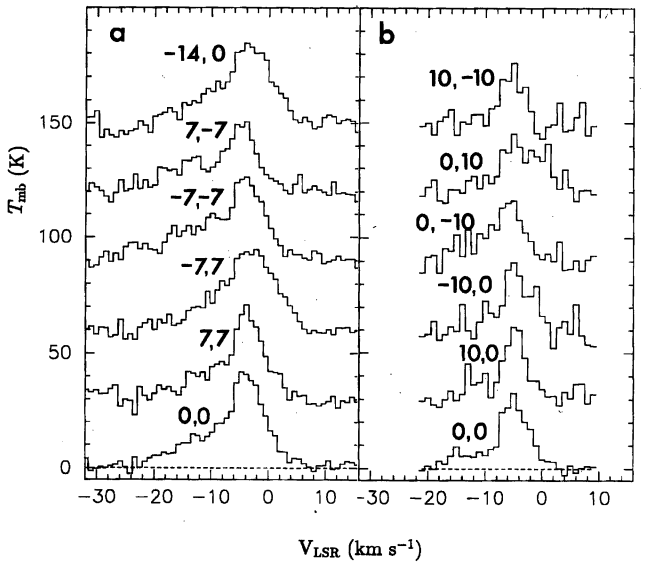

Fig. 10. Line profiles for (a) the ^{12}CO J = 3→2 transition at the 0,0 position, 7,7 (offset by +30), -7,7 (offset by +60), -7,-7 (offset by +90), 7,-7 (offset by +120) and -14,0 (offset by +150) and (b) the ^{12}CO J = 4→3 transition at the 0,0 position, 10,0 (offset by +30), -10,0 (offset by +60), 0,-10 (offset by +90), 0,10 (offset by +120) and 10,-10 (offset by +150)

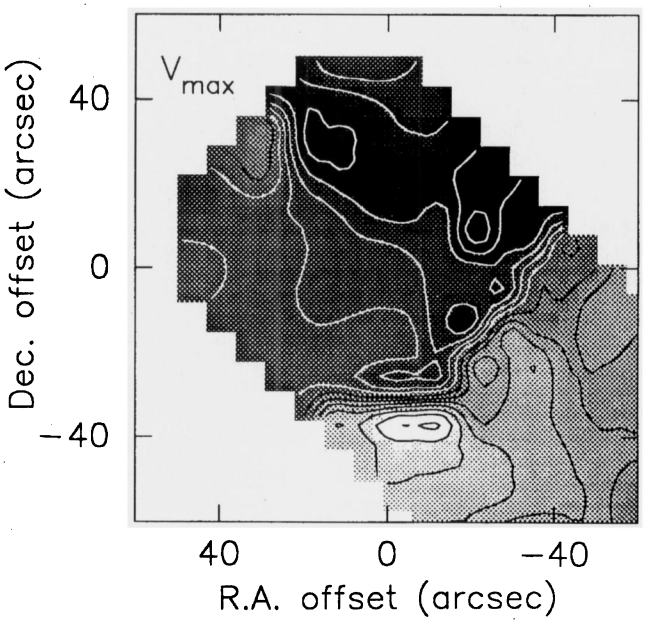

Fig. 11. Greyscale image, with contours overlaid, of V_{max}, the velocity of the line peak for the ^{12}CO J = 3→2 transition. For the greyscale image, any positions with $V_{max} \leq$-8 km s^{-1} are shown as white and any positions with $V_{max} \geq$-3 km s^{-1} are shown as black, with velocities inbetween represented as various shades of grey. The base level contour is at -8.5 km s^{-1} and the contour interval is 0.5 km s^{-1}

ular cloud is anything but quiescent. This apparent anomaly is explained if the self-absorption for velocities close to V_{LSR} ~-8 km s^{-1} (where the bulk of the self-aborption occurs) is mainly due to the ambient molecular cloud, but for the more blue and redshifted velocities the self-absorption is mainly due to the molecular outflow material itself.

The above discussion is consistent with our observations of the isotopic lines, which have distinctly lower optical depth and thus sample emission from positions right through the molecular cloud. Thus V_{max} for these lines will be close to the V_{LSR} of the ambient molecular cloud, -8 km s^{-1}, as observed. This is the same as the central velocity of the ^{12}CO self-absorption, which is to be expected if the foreground ambient molecular cloud material is responsible. Only the high velocity part of the ^{12}CO emission is transmitted through the foreground material without significant absorption.

So far we have only considered the effect of self-absorption near the (0,0) position, but from a region with embedded infrared sources and a bipolar outflow one might expect to find distinct variations in the amount of self-absorption present at different positions. Figure 11 shows a greyscale image, with contours overlaid, of V_{max} across the mapped region for the ^{12}CO J = 3→2 transition. Assuming that greater self-absorption will result in a larger shift in V_{max} from -8 km s^{-1} towards the red, then Fig. 11 should indicate the regions of greatest line-of-sight self-absorption. Ignoring the region to the extreme southwest, the PDR/ionization front interface (where the ^{12}CO emission falls off rapidly and thus the value of V_{max} found is inaccurate due to the drastically decreasing signal-to-noise) the map is composed of four distinct regions.

To the south of the (0,0) position, roughly coincident with the position of the high velocity blueshifted emission, is a region with V_{max} ~-7 to -8 km s^{-1}. To the north of the (0,0) position, roughly coincident with the position of the high velocity redshifted emission, is a region with V_{max} ~-2 to -3 km s^{-1}. The line connecting these two regions apparently forms a sharp boundary between regions to the southwest (with V_{max} ~-5.5 to -7 km s^{-1}) and northeast (with V_{max} ~-3 to -5 km s^{-1}).

The separation of the V_{max} map into these four distinct regions is not surprising. Emission from the blueshifted lobe has the smallest shift in V_{max} from the V_{LSR} of the ambient molecular cloud (~-8 km s^{-1}) as the emitting region is closest to the observer and thus emission from this region has the smallest column density of material to traverse. Conversely, emission from the redshifted lobe has the largest column density of material to traverse, and thus the largest shift in V_{max}. Emission from the region to the northeast of the line connecting the outflow lobes mainly emanates from behind the outflow and dense molecular disk. Hence there is a larger shift in V_{max} (and thus larger self-absorption) for emission from this region than for emission from the region to the southwest, between the outflow and the PDR. Of course further to the northeast one would expect V_{max} to return to the V_{LSR} of the ambient molecular cloud (~-8 km s^{-1}). This region is outside of the ^{12}CO J = 3→2 mapped area, but the ^{12}CO J = 2→1 data (which is at lower spatial resolution but has a larger mapped area) show that this is indeed the case. Examination of our ^{13}CO data shows little or no variation in V_{max} across the region, as expected for an optically thin isotope which will suffer little or no self-absorption.

4.3. *Physical properties of S140*

4.3.1. T_{mb} *cuts across the PDR*

Figure 12 shows the variation in the peak value of T_{mb} along the southwestern cut (starting at 20 arcsec to the northeast of the (0,0) position and crossing the molecular cloud/HII region interface) for each of the ^{12}CO, ^{13}CO, C^{18}O and CI transitions. The position of the ionized region is indicated by the VLA 6 cm continuum emission, taken from Fig. 2 of Evans et al. (1987).

For all six molecular transitions the peak value of T_{mb} is observed close to the (0,0) position. For the three ^{12}CO transitions T_{mb} decreases sharply either side of the (0,0) position (close to the centre of the outflow) and between +50 and +60 arcsec offset both the ^{12}CO J = 2→1 and 3→2 transitions have a local peak in T_{mb}, with a sharp dropoff to the southwest. This corresponds to the ridge feature identified on Figs. 2 and 3. The ^{12}CO J = 4→3 transition displays a much smoother decrease in T_{mb} values to the southwest of the (0,0) position, with little evidence of the ridge feature between +50 and +60 arcsec. The ^{13}CO J = 3→2, 2→1 and C^{18}O J = 3→2 transitions have a local peak in T_{mb} at between ∼+30 and +40 arcsec offset to the southwest.

The fact that the ^{13}CO and C^{18}O isotope lines peak further into the cloud than the lines of the more abundant ^{12}CO is predicted by photodissociation models (e.g. Bally & Langer 1982; Glassgold et al. 1985; van Dishoeck & Black 1988). Self-shielding of photodestructive UV transitions becomes significant when the optical depth exceeds unity, a situation rapidly achieved at the edge of the cloud for ^{12}CO, but not for the less abundant isotopes. The photodissociation rates for the isotopic species are thus larger than for ^{12}CO at the cloud edge, and hence the rarer isotopes are only able to form deeper into the cloud. It has been shown that self-shielding does reduce the ^{12}CO photdissociation rate significantly, but that because their lines are significantly shifted from those of ^{12}CO, any mutual-shielding of ^{13}CO and C^{18}O lines is not significant (van Dishoeck & Black 1988).

Values of T_{mb} are higher for the ^{12}CO J = 2→1 transition than the 3→2 transition at all points along the cut (by up to 10K), but for ^{13}CO the values of T_{mb} are higher for the J = 3→2 transition than the 2→1 transition (again by up to 10K). As the energy of the J levels is almost identical for both ^{12}CO and ^{13}CO lines, then one would expect that if the J = 2→1 line is stronger than the 3→2 line for ^{12}CO then this would also be the case for ^{13}CO. The fact that this is not so may be explained if the ^{12}CO lines are thermalised and optically thick, in which case we can use Eq. (4) where $1-e^{-\tau} \rightarrow 1$ as $\tau >> 1$.

As the column density is highest at the (0,0) position (see Sect. 4.3.2 and Fig. 14), as is T_{mb} for each of the ^{12}CO transitions, then this is the point at which the ^{12}CO lines are likely to have the highest optical depth. At this point the observed values of T_{mb} for both the ^{12}CO J = 2→1 and 3→2 transitions (44±1K and 41±1.5K respectively) are, within the errors, in agreement with those predicted by Eq. (4) for a value of T_{kin} ∼50K (44.7K and 42.2K respectively). This value for the kinetic temperature is distinctly lower than the value of T_{ex} ∼67K, derived for this position in Sect. 4.3.2 from the ^{13}CO data ($T_{ex} \rightarrow T_{kin}$ at high densities). As the line-of-sight at the (0,0) position is towards an embedded hot source it is to be expected that observations of an optically thinner isotope line will imply a higher kinetic temperature than those of optically thick ^{12}CO lines as it samples emission from regions deeper into the cloud, and thus close to the embedded infrared sources. Of course, as the ^{12}CO line profiles are affected by self-absorption, the observed peak values of T_{mb} are likely to be correspondingly reduced. Hence the derived value of T_{kin} is a lower limit and may explain the apparent difference in T_{kin} for the ^{12}CO and ^{13}CO transitions.

4.3.2. *Excitation temperature and column density cuts*

Assuming the ^{13}CO and C^{18}O lines are optically thin, we can use our data to examine the variation in T_{ex} and column density across the mapped region. Assuming LTE, the T_{mb} measurements can be related to T_{ex} and column density by

$$\frac{N}{Z(T_{ex})} = \frac{1}{e^{-E_u/kT_{ex}}} \frac{3k \int T_{mb}\, dv}{8\pi^3 \nu \mu^2 S_{ul}} \quad (5)$$

where N is the column density, μ is the dipole moment, E_u is the energy of the upper state and S_{ul} is the intrinsic strength of the transition, determined by its quantum numbers. $Z(T_{ex})$ is the partition function per magnetic sublevel and equal to hB/ kT_{ex}, where B is the rotation constant. Provided that $\tau << 1$ and T_{ex} is constant for all the J levels being considered, this equation can be solved by noting that the left-hand side is constant, so the right-hand side with the values for the J = 3→2 transition is equal to the right-hand side with the values for the J = 2→1 transition. This equality solves for T_{ex} and back-substitution gives N.

The ^{13}CO J = 3→2 and 2→1 data were used to calculate T_{ex} and N along a 70 arcsec cut extending from the origin of the maps across the ionization front towards the southwest. As the 3→2 data has a smaller beamsize (15 arcsec) than the 2→1 data (22 arcsec), these data were convolved to the larger beamsize at the same positions as the 2→1 transition data points. The values of T_{ex} derived from the ^{13}CO data were then used to calculate the column density of the C^{18}O J = 3→2 line along the same cut direction. The equation used was analogous to Eq. (1)

$$N_{C^{18}O} = \frac{T_{ex}}{e^{-31.6/T_{ex}}} 5.14 \times 10^{12} \int T_{mb}(3 \rightarrow 2)\, dv \quad (6)$$

The variations in T_{ex}, $N(^{13}CO)$ and $N(C^{18}O)$ along the southwest cut are plotted in Fig. 13, and the results are included in Table 2. As for Figs. 13(a) and (b), the position of the ionized region is indicated by the 6 cm continuum emission.

At the (0,0) position (near the infrared sources) T_{ex} is 65–70K and stays consistently around this value for the first 50 arcsec along the southwestern cut. At 56 arcsec T_{ex} increases to 80-85K, rising sharply to >250K at 70 arcsec. Although the latter data point has considerably larger errors than the other points, it suggests that enhanced heating of the layer of molecular gas adjacent to the ionization front may be present. This is also implied by the fact that the sharp increase in T_{ex} occurs at the

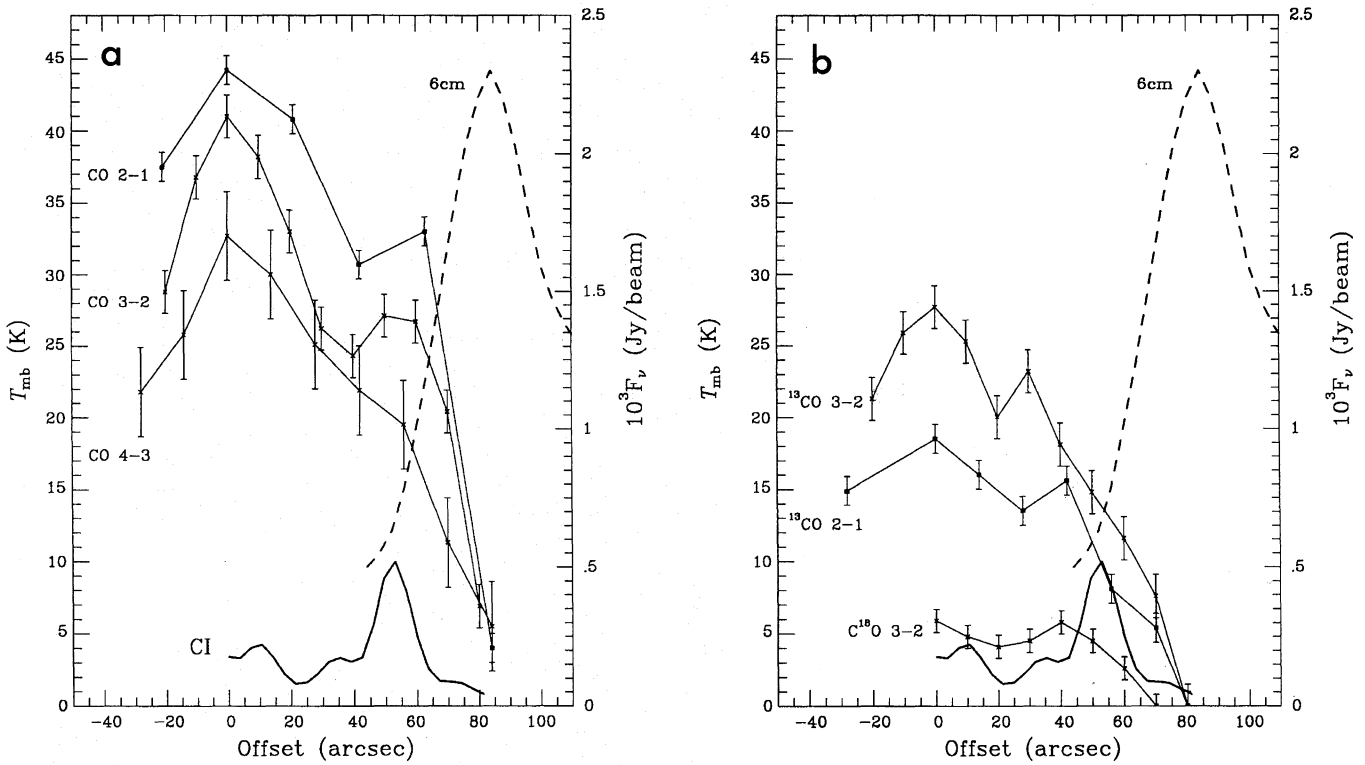

Fig. 12. The variation of T_{mb} along a cut going northeast-southwest across the (0,0) position and the molecular cloud/HII region interface for (a) the ^{12}CO J = 2→1, 3→2, 4→3 transitions and (b) the ^{13}CO J = 2→1 and 3→2 and C^{18}O J = 3→2 transitions. The CI $^3P_1 \rightarrow {}^3P_0$ emission is plotted as a bold line and the 6 cm continuum emission is plotted as a bold dashed line, with the flux density given on the right-hand axis

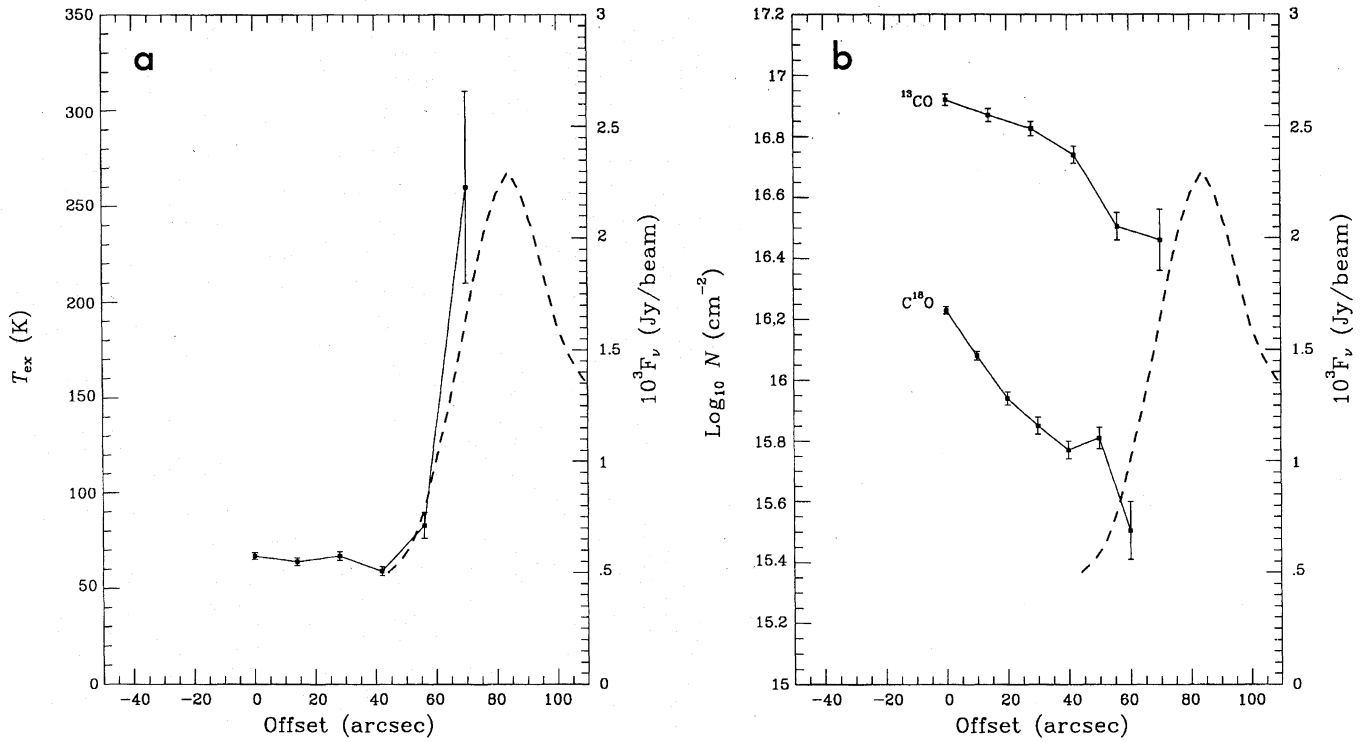

Fig. 13. The variation of (a) T_{ex} and (b) ^{13}CO and C^{18}O column density along a cut going northeast-southwest across the (0,0) position to the molecular cloud/HII region interface. The 6 cm continuum emission is plotted as a dashed line, with the flux density given on the right-hand axis

Table 2. Physical properties of the optically thin lines

Position (arcsec)	T_{ex} (K)	$N(^{13}CO)$ ($\times10^{16}$ cm^{-2})	$N(C^{18}O)$ ($\times10^{16}$ cm^{-2})	$\frac{N(^{13}CO)}{N(C^{18}O)}$
0	67±2	8.4±0.4	1.52±0.05	5.6±0.5
10			1.32±0.05	5.9±0.5
14	64±2	7.4±0.4		
20			0.92±0.04	7.7±0.7
28	67±2	6.7±0.4		
30			0.72±0.05	9.1±1.2
40			0.68±0.04	8.3±1.1
42	59±2.5	5.5±0.4		
50			0.76±0.06	5.5±1.0
56	83±7	3.2±0.5		
60			0.32±0.1	9.7±4.5
70	260±60	2.9±1.2	0.23±0.1	12.6±10.7

same point as a similar sharp rise in the 6 cm emission (between 60 and 70 arcsec). It should be noted that the beam sizes of the 6 cm and ^{13}CO maps are comparable (~20 arcsec). Enhanced heating of the layer of molecular gas adjacent to the ionization front is also consistent with the interpretation given to the ^{12}CO 'ridge' observed between 50 and 60 arcsec along the southwestern cut (Fig. 10). The derived gas temperature at the PDR/HII region interface (260±50K) is in reasonable agreement with ~200K predicted by Hollenbach et al. (1991) for a low density PDR with relatively low ultraviolet illumination ($10^2 \leq n_0 \leq 10^5$ cm^{-3} and $1 \leq G_0 \leq 10^4$). A molecular cloud, edge-illuminated by a more intense radiation field ($10^3 \leq G_0 \leq 10^6$), would produce gas temperatures up to 10^3K at the PDR/HII region interface (Tielens & Hollenbach 1985).

$N(^{13}CO)$ decreases monotonically from 8.4×10^{16} cm^{-2} at the (0,0) position to 5.5×10^{16} cm^{-2} at 42 arcsec along the cut. Between 42 and 56 arcsec the rate of decrease roughly doubles so that $N(^{13}CO)$ is 3.2×10^{16} cm^{-2} at 56 arcsec, but the drop between 56 and 70 arcsec is only 0.3×10^{16} cm^{-2} to $N_{^{13}CO}$ = 2.9×10^{16} cm^{-2} (although the errors on the 70 arcsec data point are large). $N(C^{18}O)$ also decreases monotonically (though at a faster rate than $N(^{13}CO)$) from 1.5×10^{16} cm^{-2} at the (0,0) position to 0.68×10^{16} cm^{-2} at 40 arcsec along the cut , but between 40 and 50 arcsec $N(C^{18}O)$ increases to 0.76×10^{16} cm^{-2}. From 50 to 60 arcsec $N(C^{18}O)$ again decreases, but now more rapidly to 0.32×10^{16} cm^{-2}.

The final column of Table 2 demonstrates that $N(^{13}CO)/N(C^{18}O)$ increases from 5–6 at the (0,0) position to 8–10 at +30–+40 arcsec along the cut, at the position of the localised peak in T_{mb} for the ^{13}CO and C^{18}O lines. As the empirically accepted value of [^{13}CO]/[C^{18}O] is ~5, this implies that the ^{13}CO abundance is enhanced at the edge of the cloud relative to the C^{18}O abundance. This effect has been noted previously (e.g Bally & Langer 1982) and can be attributed to a net increase in ^{13}CO due to ion-molecule exchange reactions (e.g. van Dishoeck & Black 1988). The enhancement of ^{13}CO is most significant at low kinetic temperatures (≤15K); indeed, Fig. 12 of van Dishoeck & Black (1988) shows that for T = 15K $N(^{13}CO)/N(C^{18}O)$ peaks at ~20, whilst for T = 50K $N(^{13}CO)/N(C^{18}O)$ peaks at only ~10. These latter values are in excellent agreement with those observed ($N(^{13}CO)/N(C^{18}O)$ = 8–10 and T_{ex}~65–70K).

4.4. Comparison of the molecular and atomic line data

Figure 14 displays contours of the peak main beam brightness temperature for the ^{12}CO J = 3→2 line (taken from Fig. 3) overlaid upon the greyscale image of the CI $^3P_1 \rightarrow {}^3P_0$ line (taken from Fig. 9). This figure gives qualitative confirmation of the conclusions drawn from Fig. 12, that the hot ridges of ^{12}CO and CI emission near the cloud edge are coincident and that the CI ridge is ~20 arcsec (~0.09 pc) in width, peaking ~20-30 arcsec (~0.09-0.13 pc) from the ionization front. These conclusions allow comparison of homogeneous PDR chemical models (e.g. Tielens & Hollenbach 1985; van Dishoeck & Black 1988; Hollenbach et al. 1991) and multi-component models, in which dense clumps of material are interspersed with a more tenuous inter-clump medium (e.g. Stutzki et al. 1988). S140 has a relatively low density PDR with low ultraviolet illumination (~150G$_0$), especially when compared to the archetypal edge-illuminated molecular clouds, M17 and the Orion Bright Bar (~2x10^{5}G$_0$). For this reason the model of Hollenbach et al. (1991), which considers PDRs with lower densities and FUV fluxes ($10^2 \leq n_0 \leq 10^5$ cm^{-3} and $1 \leq G_0 \leq 10^4$) than the original Tielens & Hollenbach (1985) paper, should be directly comparable. The model predicts that neutral carbon in PDRs is confined to a layer A_v~3-8 mags, between CII (adjacent to the ionization front) and ^{12}CO (deeper into the cloud).

Using the optically thin C^{18}O observations of the PDR at the position of the CI T_{mb} peak [50-60 arcsec from the (0,0) position], $N(C^{18}O)$ is between 0.32 and 0.76×10^{16} cm^{-2} (see Table 2). Assuming the S140 molecular cloud can be approximated as a sphere of ~7-8 arcmin diameter (see the large-scale ^{12}CO J = 1→0 emission map of Blair et al. 1978) and that $N(H_2)$~$5\times10^6 N(C^{18}O)$, then n(H$_2$)~2×10^4 cm^{-3} in the PDR. For regions of low extinction the molecular hydrogen column density is related to the visual extinction by $N(H_2)/A_v$ = 1.59×10^{21} cm $^{-2}$ mag $^{-1}$ (Savage et al. 1977), assuming all the hydrogen is in molecular form. Expressing this equation as n(H$_2$)$\Delta z/A_v$ = 1.59×10^{21} cm $^{-2}$ mag $^{-1}$, where Δz is the size (in cm) of the CI layer, then, assuming the CI layer extends over $\triangle A_v$~3–5 mags, Δz~20–30 arcsec.

Of course this calculation is extremely approximate, but serves to demonstrate that, for a PDR with *low* density and ultraviolet illumination, the observed spatial extent of the CI layer can be reproduced by assuming a homogeneous cloud model. Of course for a PDR with *high* density and ultraviolet illumination, such as M17, the spatial extent of the CI layer will be considerably smaller. In fact, high-spatial resolution observations of the PDR in M17 show that the CI emission is *not* confined to

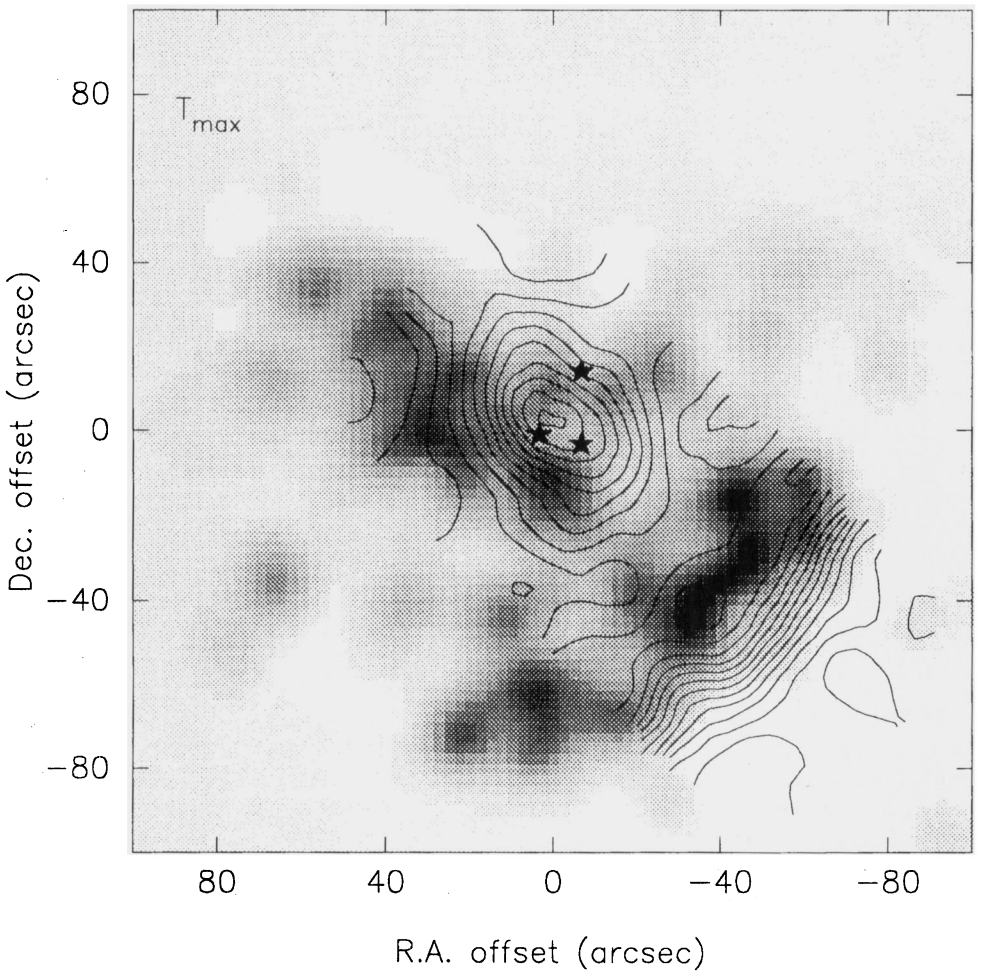

Fig. 14. Greyscale image of the peak main beam brightness temperature for the CI $^3P_1 \rightarrow {}^3P_0$ line (from Fig. 10) with isophotal contours of the ^{12}CO J = 3→2 line overlaid (from Fig. 3). The positions of the three infrared sources are shown as five-pointed stars

a layer at the PDR/HII region interface, but instead is spread throughout the molecular cloud core (White & Padman 1991). The CI emission appears to be clumpy, but comparison with $C^{18}O$ emission peaks shows the CI emission is not enhanced at the positions of highest column density for the molecular material. This is interpreted as evidence that the molecular material has high density clumps, interspersed with a more tenuous interclump medium. Thus ultraviolet radiation can penetrate deep into the cloud through the interclump medium, before dissociating ^{12}CO to produce CI at the clump edges. Such a multi-component model naturally explains why the CI emission is observed deeper into the cloud than would be expected from a homogeneous cloud model, and also the offset of the CI emission peaks from the density peaks of the molecular material.

Although the observed spatial extent of the CI emission from the PDR in S140 is consistent with both homogeneous and multi-component cloud models, there are other aspects of the observations that imply this molecular cloud, like M17, is indeed clumpy. Firstly, Figs. 9 and 14 show that the CI emission from both the PDR and deeper into the cloud has distinct, localised peaks, indicative of clumpy structure. Secondly, Figs. 13(a) and 15 demonstrate that the ridges of ^{12}CO and CI emission are coincident. This contradicts the homogeneous cloud models where CI and ^{12}CO are, to a large extent, found in adjacent layers. If the molecular material is composed of high density clumps, interspersed with a more tenuous interclump medium, then ultraviolet radiation will penetrate deep into the cloud, heating and dissociating the ^{12}CO on clump surfaces throughout the transition region. In this case we would expect to observe ^{12}CO and CI line emission from the same region at the edge of the molecular cloud.

Figures 9 and 14 show that the CI emission is also concentrated along a 'finger'-like component extending along the northeast-southwest direction. This finger component passes ~20–40 arcsec to the southeast of the (0,0) position, and thus avoids the region of intense ^{12}CO emission around the infrared sources. The tendency for CI emission to avoid the position of a bipolar outflow source has also been noted for IRc2 in the Orion Molecular cloud, where the CI appears to trace the clumpy inner edge of a cavity. A similar situation seems to be occurring here. Hayashi & Murata (1992) show that the CI and CS J = 1→0 emission peaks are offset, with the CI peaks generally located inside the CS ring (see their Fig. 7). The obvious implication is that this region of CI emission is confined within the cavity delineated by the CS ring, originating from the edges of dense clumps where the ^{12}CO molecules are primarily dissociated by the UV field from the embedded infrared cluster and *not* by the external radiation field.

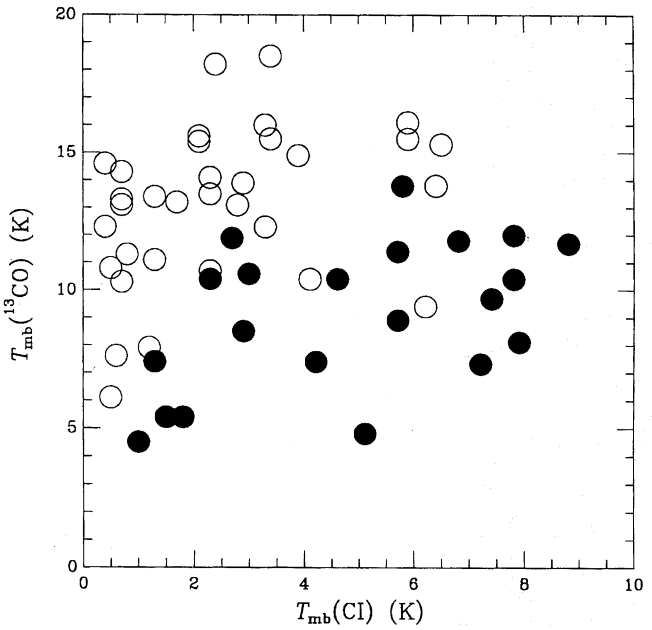

Fig. 15. The T_{mb} values for the CI $^3P_1 \rightarrow {}^3P_0$ and ^{13}CO J = 2→1 lines are plotted for each of the observed positions on the PDR (filled circles) and the rest of the molecular cloud (open circles)

White & Padman (1991) obtained CI $^3P_1 \rightarrow {}^3P_0$ line spectra at the (0,0) position and on the PDR (30 arcsec west and 45 south) and derived $N(CI)/N(^{12}CO)$ ~0.2 and 2.8 at these two positions, respectively. The ratio $N(CI)/N(^{12}CO)$ has been determined for various positions in molecular clouds over the last decade (e.g. Genzel et al. 1988; Frerking et al. 1989) including S140 (Phillips & Huggins 1981; Keene et al. 1985). For several positions across S140 (along a northeast-southwest direction, crossing the PDR) Keene et al. (1985) found that $N(CI)/N(^{12}CO)$ did not exceed 0.24 at any point. Similar values of $N(CI)/N(^{12}CO)$ (<1) have been observed towards numerous other molecular clouds. Of course these results were obtained using much larger beamwidths than the present observations (~1 arcmin compared to 9 arcsec), distinctly larger than the width of the S140 PDR (~20 arcsec).

Although our CI observations are single channel results, if we assume that the observed positions with the highest T_{mb} will also have highest column densities, then we can test whether the ratio $N(CI)/N(^{12}CO)$ is likely to be significantly higher for *all* positions on the PDR than the general molecular cloud. Figure 15 shows a graph of T_{mb} values for the CI $^3P_1 \rightarrow {}^3P_0$ line plotted against those of the ^{13}CO J = 2→1 line for each of the observed positions on the PDR (filled circles) and the general molecular cloud (open circles). Clearly the data points occupy two different regions of the graph, with little overlap. For positions on the PDR the ratio $T_{mb}(^{13}CO)/T_{mb}(CI)$ is ~1-4, whilst for the general molecular cloud $T_{mb}(^{13}CO)/T_{mb}(CI)$ ~3-15. Thus the positions on the PDR form a population which (except for a couple of points) have consistently higher values of $T_{mb}(CI)/T_{mb}(^{13}CO)$ than for the general cloud. Multi-channel observations of the CI $^3P_1 \rightarrow {}^3P_0$ line are planned to test this conclusion, and examine the velocity structure across the PDR.

5. Conclusions

We have presented high-angular resolution maps of the S140 molecular cloud in the J = 2→1, 3→2 and 4→3 transitions of ^{12}CO, the J = 2→1 and 3→2 transitions of ^{13}CO and the J = 3→2 transition of $C^{18}O$. We have also presented a single-channel map of the $^3P_1 \rightarrow {}^3P_0$ line of neutral atomic carbon (CI).

Velocity channel maps of the ^{12}CO lines show a systematic shift of the emission peak away from the outflow source with increasing velocity offset from the line centre. This may imply the bipolar outflow is accelerating with distance from the outflow source or that there is more material at high velocity further from the source, possibly due to entrainment at the working surface.

The blue and redshifted outflow lobes are separated by ~35 arcsec (0.15 pc) in projection and the outflow axis is believed to be directed close to the observers' line-of-sight. The total integrated intensity of the ^{12}CO J = 2→1 line for the blue and redshifted outflow lobes imply masses of 19.5 and 8.1$M_\odot$ respectively, giving a total mass for the outflow of 27.6$M_\odot$.

The higher J-level ^{12}CO lines are strongly self-absorbed, with the amount of self-absorption varying with position across the mapped region. In particular, the redshifted outflow lobe is more strongly self-absorbed than the blueshifted lobe, consistent with emission from this region having to traverse a larger column density of material.

All the ^{12}CO, ^{13}CO and $C^{18}O$ lines show enhanced main beam brightness temperatures near the molecular cloud/HII region interface. The fact that the ^{13}CO and $C^{18}O$ lines peak deeper into the cloud than the lines of ^{12}CO is consistent with significant self-shielding of the more abundant ^{12}CO isotope.

The ^{13}CO line intensities imply the excitation temperature increases from ~65–70K at the position of the outflow source, to ~250K at the interface region. The $N(^{13}CO)/N(C^{18}O)$ ratio is highest on the PDR (~10), consistent with enhancement of the ^{13}CO abundance due to ion-molecule exchange reactions.

The CI emission is mainly confined to a clumpy, elongated ridge-like feature adjacent to the edge of the molecular cloud and is coincident with a similar feature seen in ^{12}CO line emission. The coincidence of these features contradicts homogeneous cloud models and is interpreted as evidence that the molecular material is composed of dense clumps interspersed with a more tenuous interclump medium.

A second region of intense CI emission is located inside a ring of CS emission, implying that ^{12}CO here is dissociated by the radiation field from the embedded infrared cluster and *not* the external radiation field.

Observed positions on the PDR have significantly higher values of $T_{mb}(CI)/T_{mb}(^{13}CO)$ than for the general cloud, implying $N(CI)/N(^{13}CO)$ is likely to be significantly higher for positions on the PDR than in the general molecular cloud.

Acknowledgements. We wish to thank Kevin Richardson for providing software, Drs. G Macdonald and I. Bishop for providing a number of

additional ^{12}CO J = 2→1 spectra for the map shown in Fig. 2, Drs. N. Evans and S. Zhou for sending us their VLA 6cm data and allowing its use in this paper and Dr. J. Stutzki for his astute and helpful comments as referee. We acknowledge the SERC for travel funds, and NRM's PDRA.

References

Bally J., Langer W. D., 1982 ApJ 255, 143
Bally J., Lada C., 1983, ApJ 265, 824
Beichman C. A., Becklin E. E., Wynn-Williams C. G., 1979, ApJ Lett 232, L47
Blair G. N., Evans N. J., Vanden Bout P. A, Peters W. L., 1978, ApJ 219, 896
Crampton D., Fisher W. A., 1974, Pub. Dom. Ap. Obs. 14, 12
van Dishoeck E. F., Black J. H., 1988 ApJ 334, 771
Evans N. J., Kutner M. L., Mundy L. G., 1987, ApJ 323, 145
Frerking M. A., Keene J., Blake A., Phillips T. G., A., 1989, ApJ 344, 311
Fridlund C. V. M., White G. J., 1989, A&A 223, L13
Genzel R., Harris A. I., Jaffe D. T., Stutzki J., 1988, ApJ 332, 1049
Glassgold A. E., Huggins P. J., Langer W. D., 1985, ApJ 290, 615
Graf U. U., Genzel R., Harris A. I., Hills R. E., Russell A. P. G., Stutzki J., 1990, ApJ 358, L49
Hackwell J. A., Grasdalen G. L., Gehrz R. D., 1982, ApJ 252, 250
Hayashi M., Omadaka T., Hasegawa T., Suzuki S., 1985, ApJ 288, 170
Hayashi M., Hasegawa T., Omadaka T., Hayashi S. S. Miyawaki R. 1987, ApJ 312, 327
Hayashi M., Murata Y., 1992, PASJ 44, 391
Hollenbach D. J., Takahashi T., Tielens A. G. G. M., 1991, ApJ 377, 192
Jaffe D. T., Genzel R., Harris A. I., Lugten J. B., Stacey G. J., Stutzki J., 1989, ApJ 344, 265
Keene J., Blake A., Phillips T. G., Huggins P. J., Beichman C. A., 1985, ApJ 299, 967
Minchin N. R., Hough J. H., McCall A., Aspin C., Yamashita T., Burton M. G., 1991a, MNRAS 249, 707
Minchin N. R., Hough J. H., McCall A., Aspin C., Hayashi S. S., Yamashita T., Burton M. G., 1991b, MNRAS 251, 508
Minchin N. R., Ward-Thompson D., White G. J. 1992 A&A, 265, 733
Padman R., White G. J., Barker R., Bly D., Johnson N., Gibson H., Griffin M., Murphy J. A., Prestage R., Rogers J., Scivetti A., 1992, Intl. Jour. of IR and mm Waves 13, 1487
Parker N., White G. J., Hayashi S. S., Williams P. G., 1991, A&A 250, 134
Phillips J. P., White G. J., Rainey R., Avery L. W., Richardson K. J., Griffin M. J., Cronin N. J., Monteiro T., Hilton J., 1988, A&A 190, 289
Phillips T. G., Huggins P. J., 1981, ApJ 251, 533
Richer J. S., 1992, MNRAS 254, 165
Richer J. S., Hills R. E., Padman R., 1992, MNRAS 254, 525
Sato S., Nagata T., Nakajima T., Nishida M., Tanaka M., Yamashita T., 1985, ApJ 291, 708
Snell R. L., Mundy L. G., Goldsmith P. F., Evans N. J., Erickson N. R., 1984a, ApJ 276, 625
Snell R. L., Scoville N. Z., Sanders D. B., Erickson N. R., 1984b, ApJ 284, 176
Stutzki J., Stacey G. J., Genzel R., Harris A. I., Jaffe D. T., Lugten J. B., 1988, ApJ 332, 379
Tielens A. G. G. M., Hollenbach D. J., 1985, ApJ 291, 722
Uchida Y., Kaifu N., Shibata K., Hayashi S. S., Hasegawa T., 1987, In: Star Forming Regions, IAU Symp. No. 115, eds. Peimbert M., Jugka J., Reidel, Dordrecht, p. 287
White G. J., Phillips J. P., Richardson K. J., Harten R. H., 1986 A&A 159, 309
White G. J., 1988, In: Millimetre and Submillimetre Astronomy, eds. Wolstencroft R. D., Burton W. B., Kluwer, p. 27
White G. J., Padman R., 1991, Nat 354, 511

This article was processed by the author using Springer-Verlag LaTeX A&A style file version 3.